Effect of H^+ Exchange & Surface Impurities on Bulk & Interfacial Electrochemistry of Garnet Solid Electrolytes

Sunny Wang,[†,‡,¶] Edward Barks,[§,‡,¶] Po-Ting Lin,[§] Xin Xu,[§,‡] Celeste Melamed,[§,‡] Geoff McConohy,[§,‡] Slavomír Nemšák,[‖,⊥] and William C. Chueh[*,§,‡,#]

†*Department of Chemistry, Stanford University, Stanford, CA 94305, USA*

‡*Stanford Institute for Materials and Energy Science, SLAC National Accelerator Laboratory, Menlo Park, CA 94025, USA*

¶*These authors contributed equally to this work*

§*Department of Materials Science and Engineering, Stanford University, Stanford, CA 94305, USA*

‖*Advanced Light Source, Lawrence Berkeley National Laboratory, Berkeley, California 94720, USA*

⊥*Department of Physics and Astronomy, University of California, Davis, CA 95616, USA*

#*Department of Energy Science & Engineering, Stanford University, Stanford, CA 94305, USA*

E-mail: wchueh@stanford.edu

Abstract

Contact loss and current constriction pose significant challenges at the Li metal interface of solid-state batteries. For garnet-structured $Li_7La_3Zr_2O_{12}$ (LLZO), these effects are amplified by Li^+/H^+ exchange and surface contamination reactions, which lead to conductivity losses and poor Li wetting. In this study, we utilize a variety of surface treatment processes across

https://doi.org/10.26434/chemrxiv-2024-nxtpf **ORCID:** https://orcid.org/0000-0003-2210-8226

37 cells to selectively induce proton exchange and contamination reactions in LLZO. The resulting bulk and surface chemistry is systematically characterized and correlated to changes in electrochemical properties. Additionally, we combine impedance analysis and finite element method modeling to deconvolute sources of impedance contributions at the Li metal interface. Specifically, we show that constriction impedance at the Li metal interface arises not solely from voids, but also from ionically-resistive surface contaminants. These findings emphasize the connection between ionic conductivity and constriction, demonstrating that micron-scale ionically-resistive components increase constriction even with identical contact geometries. Finally, we leverage our comprehensive dataset to highlight unstable overpotential growth as a failure mechanism, additionally showing that the phase of a cell's impedance is a sensitive indicator for the onset of interfacial instability. Overall, this study clarifies the impacts of proton exchange and surface contamination on electrochemical properties at the Li|solid electrolyte interface and elucidates insights that are generalizable to other solid-state battery systems.

Introduction

Global efforts to electrify transportation and provide grid level energy storage have driven demand for new battery technologies with improved safety, power density, and energy density [1,2]. One promising strategy is the development of solid-state batteries (SSBs) which potentially offer improved safety characteristics [3,4] and greater compatibility with energy-dense negative electrode materials such as Li metal [5,6] compared to conventional batteries utilizing liquid electrolytes.

Amongst solid electrolyte (SE) chemistries, doped cubic $Li_7La_3Zr_2O_{12}$ (LLZO) has garnered significant attention as a separator material due to its high bulk ionic conductivity and minimal chemical reactivity with Li metal [7–10]. Despite this apparent stability in contact with Li metal, LLZO suffers from other surface reactions under common processing conditions. It is well known that LLZO undergoes Li^+/H^+ exchange in the presence of protic solvents, such as water vapour in air [11–23]. Neutron diffraction [19] and transmission electron microscopy [15] studies have shown that protons insert into the Li^+ sites of LLZO without modifying the cubic crystal structure. In air, Li^+/H^+ exchange results in the formation of surface contaminants, such as LiOH and Li_2CO_3, as summarized by the following equations:[17,24,25]

$$Li_7La_3Zr_2O_{12} + xH_2O \rightarrow Li_{7-x}H_xLa_3Zr_2O_{12} + xLiOH \tag{1}$$

$$2LiOH + CO_2 \rightarrow Li_2CO_3 + H_2O. \tag{2}$$

Equation 1 is also written in Kröger Vink notation as $Li_{Li}^{\times} + H_2O \rightarrow H_{Li}^{\times} + LiOH$. These surface reactions cause myriad detrimental effects at the Li|LLZO interface. First, the presence of lithiophobic species such as Li_2CO_3 induces poor interfacial contact. Contact loss then leads to current constriction and large overpotentials during cell cycling that exacerbate Li intrusion in the SE and subsequent failure via short circuiting[24,26,27]. Second, Li^+ loss as a result of proton exchange has been reported to diminish the conductivity of LLZO[11,18,19] and introduce a resistive, proton-rich interlayer[28]. As constriction is directly tied to bulk properties of the electrolyte, a decrease in LLZO ionic conductivity increases both bulk and constriction impedance in the system[29].

Substantial work has been done to understand and mitigate contamination reactions on the surface of LLZO. Treatment methods such as polishing[24], high-temperature annealing[24,30,31], acid treatment[32–34], and chemical protonation followed by deprotonation[35] have been investigated as pathways for engineering a low-resistance Li|LLZO interface. Proton exchange is of particular importance given the prevalence of protic solvents in surface treatments and processing methods (e.g., tape casting[36–39]). In evaluating these treatments, many cell cycling studies emphasize critical current density (CCD), the current density at which a cell fails as a result of short circuiting, as a key performance metric. However, CCD is an amalgamation of multiple dynamic processes during cell cycling and is highly sensitive to cycling conditions, which are not standardized in literature[40–42]. Additionally, SSBs can fail from other mechanisms beyond short-circuiting; an equally limiting process is contact loss and unstable overpotential growth at the Li|SE interface as a result of Li stripping[43–45].

In this work, we systematically investigate surface contamination reactions on high density (98.9%) $Li_{6.6}La_3Zr_{1.6}Ta_{0.4}O_{12}$ by varying the SE processing conditions. Inspired by work demonstrating the inherent variability when testing SSBs[46], each condition is examined through $n \geq 4$ replicates to ensure internal consistency, encompassing a total of 37 cells. The resultant surface chemistry is comprehensively characterized and correlated to bulk and interfacial electrochemical properties at the Li|LLZO interface. We employ a combination of treatment methods, summarized in Figure 1, to prepare LLZO samples with varying levels of surface contamination and proton exchange. Specifically, polishing and heat treatment are used to remove surface contaminants on LLZO, while exposure to solutions with varied Li^+ and H^+ activities is used to induce different extents of Li^+/H^+ exchange. Following surface treatments, we utilize a series of techniques including near ambient pressure X-ray photoelectron spectroscopy (NAP-XPS) and time-of-flight secondary ion mass spectrometry (ToF-SIMS) to characterize the surface chemistry and proton exchange level of LLZO. Electrochemical impedance spectroscopy (EIS) and cell cycling reveal the impact of these changes on the electrochemistry of LLZO. We provide a detailed understanding of the different impedance contributions in Li|LLZO|Li symmetric cells, including evidence for constriction derived from ionically-resistive layers at the Li|LLZO interface. These insights are supplemented by finite element method (FEM) calculations, which model constriction scenarios at SSB interfaces. Finally, we demonstrate the importance of unstable overpotential growth from Li metal contact loss as a failure mechanism that limits practical operating current densities before short circuiting events.

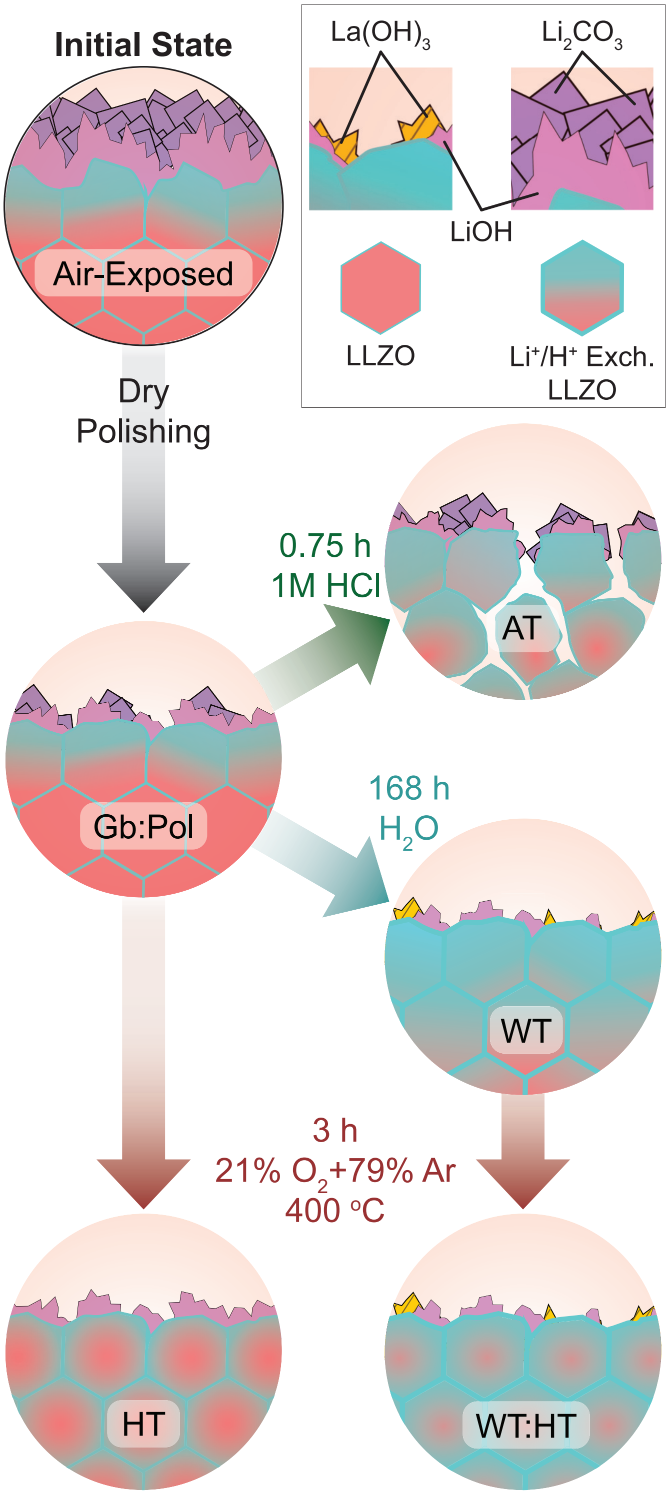

Figure 1: Schematic summarizing the surface treatments employed in this study and how they impact the surface chemistry, proton exchange, and surface morphology of LLZO. Acronyms are defined in the Experimental section.

Experimental Section

LLZO Sample Preparation

Ta-doped LLZO ($Li_{6.6}La_3Zr_{1.6}Ta_{0.4}O_{12}$) was acquired from Toshima Manufacturing Company in the form of pressed pellets (16 mm diameter, 1 mm thickness). Relative density, calculated geometrically, is 98.9% of theoretical (Table S2). X-ray diffraction confirmed phase purity. Once received, each pellet was sanded on a polishing wheel (Buehler Simplimet 2000) at 150 RPM with an incremental series of polishing materials (240 grit, 400 grit, 600 grit, 800 grit, 1200 grit SiC sanding discs; 6 μm, 1 μm diamond suspensions). Surface uniformity was monitored via optical microscopy (Leica DM4000 M) to minimize the presence of polishing defects. Once both faces were polished, the pellets were brought into an Ar-filled glovebox (O_2 and $H_2O < 0.5$ ppm) and cut into 3.175 mm x 3.175 mm squares for subsequent testing using a custom-made scoring alignment jig. Prior to surface treatments, LLZO pellets were additionally polished using 1 μm lapping film inside the glovebox.

After every pellet underwent the aforementioned dry-polishing, samples were selectively modified with a combination of surface treatments; samples without further treatment are described as glovebox polished (Gb:Pol). For Water Treatment (WT), a LLZO pellet was placed into 15 mL of deionized (DI) water for 7 days. For Acid Treatment (AT), a LLZO pellet was placed into 100 mL of 1M HCl for 45 minutes. For LiOH Treatment (LiOH:HT), LLZO was placed into 15 mL of 3M LiOH for 1 week. For Heat Treatment (HT), LLZO was placed in a custom alumina crucible with both faces exposed before being sealed inside a 1” alumina tube with airtight gasket fittings at both ends. This tube was placed inside a custom furnace within the Ar glovebox, and the inlet and outlet gas lines were connected to 21% O_2+79% Ar and an exhausted vent line, respectively. The gas flow rate was set to 100 sccm using a mass flow controller (MKS, M100B01322CS1BV) for the duration of heating, and the tube was purged with pure Ar before cooling down. The heating protocol consisted of a 7 °C min^{-1} ramp to 430 °C and a three hour hold at 430 °C.

NAP-XPS Heating Experiments

NAP-XPS measurements were performed on beamline 9.3.2 at the Advanced Light Source at Lawrence Berkeley National Laboratory. LLZO samples and Au foil were mounted onto a ceramic heating stage with the surface temperature monitored via a clip-mounted thermocouple. A R4000 HiPP electron analyzer was differentially pumped with the flow rate of gas manually adjusted to maintain an approximate chamber pressure of 500 mTorr for all Ar and O_2 heating measurements. All measurements were performed at a nominal X-ray beam energy of 730 eV with additional scans at 750 eV to check for Auger contributions.

Lab XPS Experiments

Lab-based XPS measurements were performed on a Phi VersaProbe 4 XPS system with a monochromated Al Kα X-ray source. Sputtering was conducted using a 1 mm × 1 mm monoatomic Ar^+ ion gun with voltage and current settings of 1 kV and 1 µA, respectively. This setting was been calibrated to a sputtering rate of $3\,\mathrm{nm\,min^{-1}}$ on Si.

XPS Data Analysis

Peak fitting was performed using CasaXPS[47]. Au in electrical contact with LLZO was used as an absolute reference to establish the C 1s and Zr $3d_{5/2}$ binding energies of a Li_2CO_3-contaminated LLZO surface (Figure S1). The Zr $3d_{5/2}$ peak at 180.7 eV is used as an internal reference for all LLZO samples exhibiting a discernible Zr signal while the C 1s Li_2CO_3 peak at 289.8 eV is used to reference contaminated LLZO samples without detectable Zr. We note that while charge referencing is commonly conducted using the C 1s peak of adventitious carbon, this peak is not present for LLZO surfaces heated in O_2. Furthermore, the adventitious carbon C 1s peak is potentially an inconsistent reference due to differential charging effects and variations in binding energies for different carbon species[48,49].

We fit backgrounds for O 1s, C 1s, Li 1s, and Zr 3d core scans using a Shirley background, while a 3-parameter Tougaard background was used for La 3d scans. Peak fitting was conducted using Gaussian Lorentzian peak shapes with an asymmetric tail introduced for π-bonded carbon species in Ar-heated LLZO in the NAP-XPS measurements. Peak area constraints according to spin orbit coupling were applied for appropriate core level scans. Correlation plots from NAP-XPS were obtained via linear regression on the integrated peak areas from XPS fitting. Correlation plots were only calculated from measurements obtained in the same gas environment.

Electron Microscopy

Scanning electron microscopy (SEM) images were collected using a Thermo Fisher Scientific Apreo SEM and a FEI Helios NanoLab 600i FIB/SEM system. All SEM images and videos were collected using an acceleration voltage of 2 kV and beam current of 86 pA. A custom-built vacuum transfer vessel was used to transfer all samples from the glovebox to SEM instruments in order to minimize air exposure. SEM images presented in the text were algorithmically contrast/brightness corrected by first normalizing the range of the data to cover 85% of the dynamic range of the data then applying an offset to set the mean pixel value to 35% of the maximum allowable data value. Corrections were limited to first-order alterations to avoid misrepresenting the images.

ToF-SIMS

ToF-SIMS was conducted by Infinita Labs and Tascon. Samples were prepared via the methods discussed above and were sealed in multiple layers of environmental protection while inside an Ar-filled glovebox before being shipped for analysis. Characterization was conducted on an IONTOF TOF-SIMS5-300; the sputtering ion was Cs^+ at 2 keV, and the analysis ion was Bi_3^+ at 30 keV. Sputtering time was converted to depth via post-analysis of the crater using optical profilometry (Sensofar PLu neox). For analysis, the ToF-SIMS depth profiles were split into three segments: surface contamination, near-surface, and bulk. All samples were exposed to air prior to measurement and therefore accumulated varying levels of contamination on the surface; in order to compare all samples on an equal basis, the depth at which a rolling mean of $\frac{\partial}{\partial z}\mathrm{LaO}^+$ passed through zero was chosen to indicate when the bulk LLZO had initially been reached, and this depth was set to zero for comparing between samples. The LaO^+ signal is strong and not present in the surface layer, making it an ideal reference signal. The bulk of the sample was further identified by finding the depth at which the $^6Li^+$ intensity plateaued. Each individual species to be compared was normalized by dividing the species intensity data by the average intensity of the same species in the LLZO bulk. Since the H^+ signal approached the detection limit of the tool in the bulk region, the H^+ data was normalized by the $^6Li^+$ average bulk intensity. The normalized H^+ data was further standardized by subtracting the mean of the normalized H^+ intensity in the bulk. This process was modeled after existing ToF-SIMS analysis in literature[50].

Electrochemical Characterization

EIS and cell cycling measurements were performed on Li symmetric cells assembled in a Ar glovebox dedicated for LLZO (Mbraun Labstar). Li metal used for electrodes was first purified by melting Li on a hotplate then removing accumulated surface films using a stainless steel brush. This was repeated until the surface contamination layer was replaced with a lustrous Li surface. Electrodes were punched out from the purified Li metal and assembled into a cell with the surface treated LLZO. A Kapton mask with a 2.4 mm circular opening sat between Li metal and LLZO, and the current-collectors had a corresponding 2.29 mm protrusion to ensure a constant electrode contact area. The cell assembly was then heated at 200 °C to melt Li and improve cell contact. After heating, the cells were sealed in aluminum pouches, placed between two steel plates that applied 10 MPa of pressure via four perimeter springs, and brought outside the glovebox for electrochemical tests.

All EIS measurements were performed using a Biologic SP300 potentiostat operating between 7 MHz and 30 mHz. Potentiostatic EIS measurements, with an excitation amplitude of 10 mV, were performed on all cells before and after cell cycling. For current-biased galvanostatic EIS measurements, a DC current bias was applied on top of the AC excitation amplitude. Measurements with the reverse bias were performed between each successive measurement in order to check for instability and restore interfacial contact. Distribution of relaxation times (DRT) and equivalent circuit fitting were performed using Python code based off DRT Tools[51] and LMFIT Python packages[52]. Effective capacitance values were extracted from constant phase elements using Equation 3[53].

$$C_{eff} = Q^{\frac{1}{\alpha}} R_{\parallel}^{\frac{1-\alpha}{\alpha}} \tag{3}$$

Here, Q and α are constant phase element parameters and $R_{\parallel}$ represents the resistance in parallel.

LLZO symmetric cells were cycled on PARSTAT PMC-1000 (Ametek Scientific Instruments) inside a temperature-controlled chamber (Amerex IC150R) held at 30 °C. The cells were stabilized in the chamber for 3 h prior to cycling. The cycling protocol consisted of (i) five initial formation cycles at $0.01\,\mathrm{mA\,cm^{-2}}$ for one hour per half-cycle, (ii) one cycle at $0.05\,\mathrm{mA\,cm^{-2}}$ for $1\,\mathrm{mAh\,cm^{-2}}$ per half-cycle, and (iii) segments of three cycles at a constant current density $0.05\,\mathrm{mA\,cm^{-2}}$ higher than the previous current density for $1\,\mathrm{mAh\,cm^{-2}}$ per half cycle. Step (iii) was repeated until the cell failed via disconnection (reaching the voltage compliance limit of ±10.05 V on the PMC-1000) or short-circuiting (cell potential falls precipitously to approximately zero). An alternating sequence of EIS (1 MHz to 100 mHz, 10 mV perturbation amplitude) and open-circuit steps were placed between each half-cycle to observe the impedance changes between plating and stripping while the cell was at rest.

Constriction Impedance Simulations

Finite element method calculations for constriction impedance were performed on COMSOL Multiphysics using an AC/DC package and repeated on the general PDE package. Further details are described in the Supplementary Information (SI).

Results

NAP-XPS Heating Under Different Gas Environments

To establish quantitative speciation of chemical components and optimize annealing conditions for contaminant removal, we performed NAP-XPS on LLZO pellets heated in different gaseous environments. Figures 2a and 2b depict select O 1s, C 1s, Zr 3d, and Li 1s spectra of air-exposed LLZO pellets heated from room temperature to 400 °C in 500 mTorr O_2 and separately in 500 mTorr Ar. All XPS measurements were acquired using an incident X-ray beam energy of 730 eV, corresponding to an information depth $\leq 2\,\mathrm{nm}$ (see Table S1 in the SI for electron escape depth calculations). Further details regarding NAP-XPS data collection, charge referencing, and data analysis are described in the Experimental section.

We validate XPS peak assignments by correlating O 1s, Li 1s, and C 1s photo-emission peak areas attributed to a specific chemical species. For example, Figure 2c plots the area of the LLZO O 1s peak (528.7 eV binding energy) against the area of the LLZO Li 1s peak (52.0 eV binding energy) at different temperatures during heating in O_2. The high correlation coefficient (R=0.954) from linear regression indicates that these peaks originate from the same source and that the LLZO

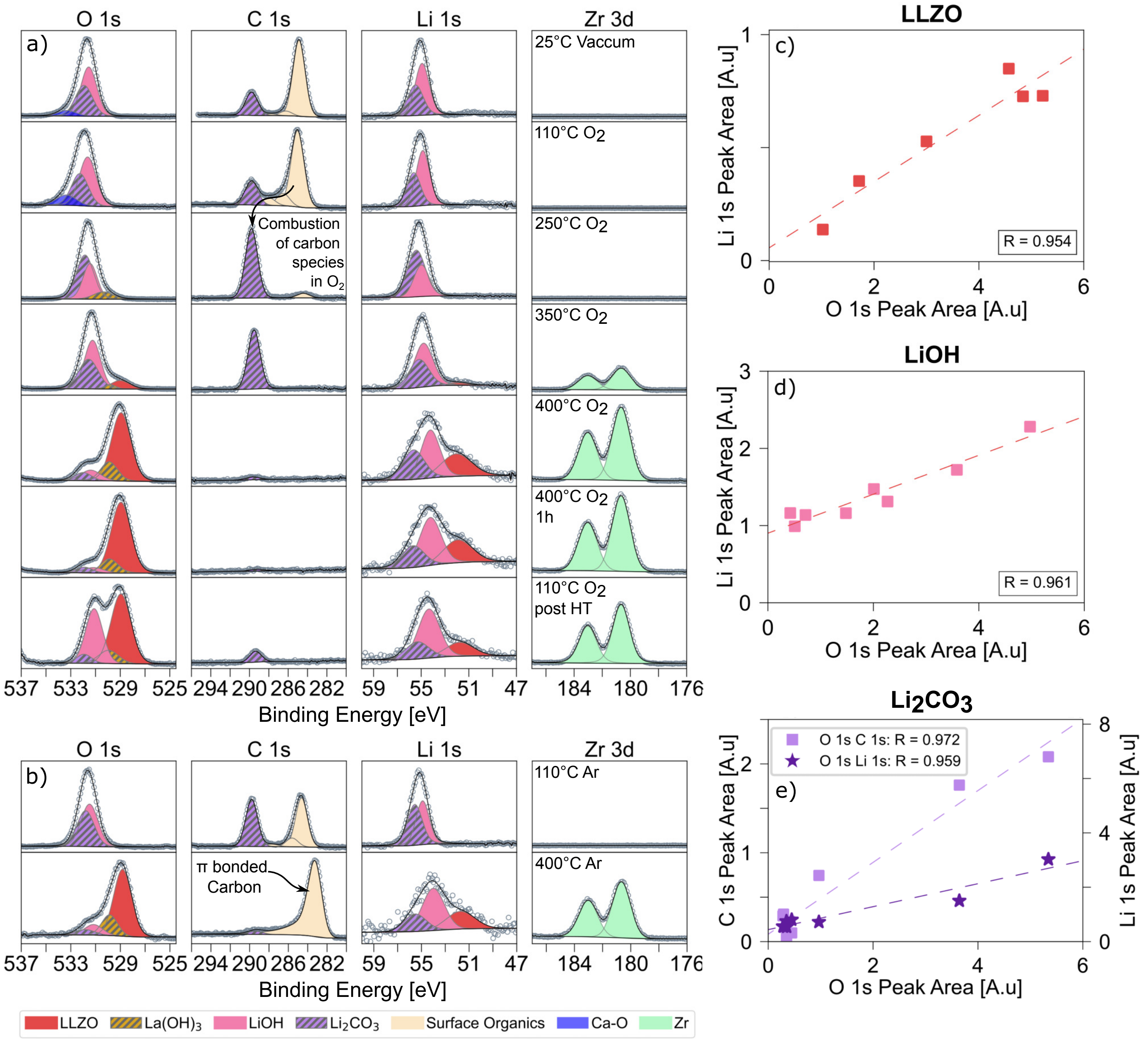

Figure 2: Select in situ NAP-XPS data of separate polished LLZO samples heated in **(a)** 500 mTorr O_2 and **(b)** 500 mTorr Ar. All temperatures are reported to 2 significant figures. C 1s and Zr 3d data are plotted on the same y-axis range for identical gas environments. In the O 1s spectrum, the peaks at 531.8 eV, 531.3 eV, and 528.7 eV are assigned to Li_2CO_3, LiOH, and LLZO, respectively. In the Li 1s spectrum, these compounds are assigned to peaks at 55.5 eV, 54.7 eV, and 52.0 eV, respectively. Li_2CO_3 shows an additional C 1s peak at 289.8 eV. We note that the LLZO peak at 52.0 eV likely contains contributions from both Li 1s and Zr 4s; however, due to difficulties in deconvoluting these features, they are not considered separately. **(c)-(e)** O 1s, C 1s and Li 1s peak area correlation plots for LLZO, LiOH, and Li_2CO_3 species, respectively, during in situ heating experiments in 500 mTorr O_2. Slight deviations from linearity may arise due to differences in the O 1s, C 1s, and Li 1s information depths (Table S1), which also account for the non-zero intercepts from linear regression.

peak assignments are self-consistent. Similar correlation plots were constructed for LiOH (Figure 2d), Li_2CO_3 (Figure 2e), and species from heating in Ar (Figure S6), which support the XPS peak assignments for these compounds.

The evolution of chemical species in Figure 2a demonstrates the effectiveness of heat treatment in O_2 for removing surface contaminants. The main contaminants observed at 25°C in vacuum prior to heating are Li_2CO_3 and LiOH, consistent with previous XPS measurements on air-exposed LLZO[10,24]. We observe no significant changes to the surface composition until the sample is heated to 250 °C. The combustion of surface organics at $T \geq 200\,°C$ in O_2 produces CO_2, which causes significant Li_2CO_3 formation via Equation 2. Further heating leads to the near-complete removal of LiOH and Li_2CO_3, with a notable decrease in contaminants when transitioning from 350 °C to 400 °C; this decrease is accompanied by the appearance of photoemission peaks attributed to LLZO, in particular an increase in Zr 3d signal. The removal of these surface contaminants at $T \geq 350\,°C$ is consistent with previous NAP-XPS studies[31] and density-functional theory calculations which indicate that the reversal of reactions 1 and 2 is thermodynamically favorable above 300 °C[25].

However, the contaminant-free LLZO surface is not preserved after cooling—significant quantities of LiOH and trace amounts of Li_2CO_3 are observed upon returning to 110 °C due to the entropic driving force of adsorption. Mass spectrometry data collected simultaneously inside the NAP-XPS chamber (Figure S7c) show that the counts for H_2O and CO_2 fragments are over 3 orders of magnitude lower than those for O_2 held at a pressure of 500 mTorr. LLZO heating experiments conducted in H_2S- and SO_x- contaminated chambers (Figure S7a) also demonstrate that sulfate contamination readily occurs on LLZO surfaces above 300 °C. These results suggest that a contaminant-free LLZO surface can only be maintained at elevated temperatures or under ultra-high vacuum.

Additional LLZO heating experiments were conducted in 500 mTorr Ar (Figure 2b). Similar to the results in O_2, heating to 400 °C in Ar results in the near-complete removal of LiOH and Li_2CO_3. However, the absence of O_2 prevents the combustion of surface organics. Comparisons between the C 1s spectra at 110 °C and 400 °C show that heat treatment in Ar leads to carbon deposition and pyrolysis on LLZO. The presence of an asymmetric tail and shift to lower binding energies for the main surface organic peak is consistent with π-bonded carbon species[48,49], which has also been reported in other LLZO heating experiments in Ar[31]. In summary, our NAP-XPS results demonstrate that heating to 400 °C in either Ar or O_2 removes contamination from LLZO; furthermore, O_2 is essential for combusting surface organics but can also lead to sulfate contamination if sulfur species are present in the gas environment.

Effect of Surface Treatments on LLZO Surface Chemistry & Morphology

Informed by the NAP-XPS measurements, we used lab-based XPS to characterize how surface treatments systematically modify the LLZO surface chemistry. These results are presented in Figure 3 alongside topographical changes observed in SEM. All samples were transferred in air-free containment from the glovebox to XPS and SEM instruments to minimize contamination.

Cleaved LLZO

We first establish the surface chemistry and morphology for untreated LLZO by considering an unaltered surface created by cleaving a pellet inside an Ar glovebox (O_2 and $H_2O \leq 0.5$ ppm). The SEM image of the cleaved surface (Figure 3g) reveals a highly-densified poly-crystalline LLZO with grain sizes ranging between 2 and 5 µm. Lab-based XPS data for the cleaved surface (Figure 3a) show clear contributions from LLZO with no photoemission peaks associated with Li_2CO_3 (fitted using peak assignments determined from NAP-XPS). However, significant quantities of LiOH are present on the cleaved surface as a result of Li^+/H^+ exchange (Equation 1). The high coverage of LiOH on the Li^+-rich cleaved surface is surprising given the minimal exposure to the glovebox Ar environment (≤ 10 min) before XPS analysis. These XPS results underscore the moisture sensitivity of LLZO (i.e., a highly-favorable adsorption energy)—a controlled environment with sub–parts per million concentration of water is insufficient for maintaining a contaminant-free surface.

Glovebox Polished LLZO (Gb:Pol)

Figure 3b presents XPS data of an air-exposed LLZO pellet that was dry polished in air and again in a glovebox (see Experimental section for details). Comparison to an identically air-exposed pellet not subjected to dry polishing (Figure S8a) shows that polishing effectively removes Li_2CO_3 and results in trace quantities of LLZO being detectable. Nonetheless, contaminants such as LiOH

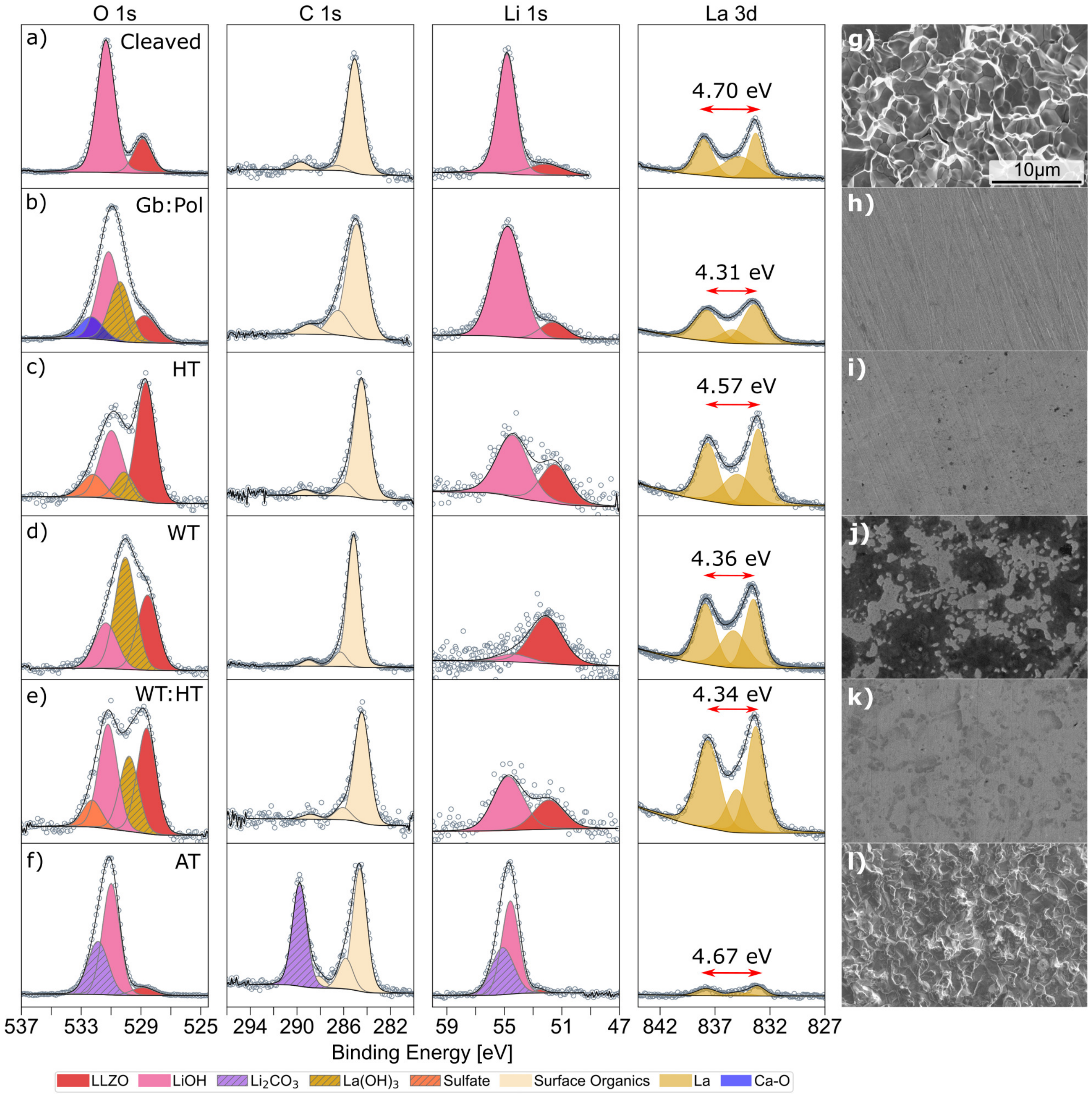

Figure 3: Lab-based XPS and SEM of LLZO surfaces having undergone different surface treatments. **a), g)** Cleaved LLZO surface. **b), h)** Polished inside a glovebox. **c), i)** 3 h heat treatment in 21% O_2 + 79% Ar at 430 °C. **d), j)** 1 week exposure in DI water. **e), k)** 1 week exposure in DI water + heat treatment in 21% O_2 + 79% Ar at 430 °C. **f), l)** 45 minutes exposure in 1M HCl. All samples except the cleaved surface were subjected to the same polishing procedure as Gb:Pol LLZO prior to surface treatment. La 3d intensities were normalized using the average of 10 pre-edge background points[54] and plotted on the same y-axis range for comparison. Annotations on the La 3d spectra denote the separation between the La $3d_{5/2}$ peak and charge-transfer satellite. This separation is highly sensitive to the the La bonding environment and notably smaller in La-OH type environments (e.g., $La(OH)_3$) versus La-O type environments (e.g., La_2O_3 or LLZO)[55].

still dominate the surface composition, illustrating that polishing alone cannot effectively clean the surface. The SEM image in Figure 3h demonstrates that polishing produces a flat surface with no clear distinction between grains and grain boundaries. We note that ceramics are often wet-polished; however, wet polishing using water exposes the grain structure of LLZO and appears to dislodge grains via grain boundary erosion (Figure S9).

Heat Treated LLZO (HT)

Heat treated LLZO was prepared by annealing a polished LLZO pellet under flowing 21% O_2 + 79% Ar for 3 hours at 430 °C in a tube furnace inside a glovebox. Figure 3c shows that heat treatment effectively removes Li_2CO_3 and some LiOH, leading to a higher proportion of LLZO being revealed compared to the polished surface. The presence of LiOH is attributed to Li^+/H^+ exchange inside the glovebox after heat treatment and is consistent with the NAP-XPS results, which show re-contamination post–heat treatment. SEM of HT LLZO (Figure 3i) indicates that heat treatment maintains the surface morphology but exposes more surface asperities (e.g., pits) compared to the Gb:Pol surface.

Water Treated LLZO (WT)

Figure 3d shows the XPS data of a polished LLZO pellet that was subsequently immersed in DI water for 168 h; this water treatment removes Li_2CO_3 via dissolution and reveals more LLZO at the surface compared to both cleaved and polished samples. WT concurrently forms $La(OH)_3$, which has been observed using X-ray diffraction[14] and infra-red spectroscopy[12] for water-exposed LLZO powder. $La(OH)_3$ formation is corroborated by the decreased La 3d peak separation in water-exposed samples compared to non-water-exposed samples (e.g., WT vs. HT LLZO), reflecting the different La bonding environments in $La(OH)_3$ and LLZO[55]. Furthermore, water treatment induces significant carbon accumulation on the surface as reflected by the high C 1s counts in XPS survey scans (Figure S10) and dark patches in SEM (Figure 3j). Ar^+ sputtering on WT LLZO (Figure S11d) increases the La 4d separation from 4.36 eV to 4.66 eV while also removing LiOH and surface carbon species. Therefore, $La(OH)_3$, surface organics, and LiOH appear to be confined to a nanometer-scale-thick surface layer on the WT sample.

Water Treated + Heat Treated LLZO (WT:HT)

Figure 3e shows XPS data on WT LLZO that was additionally heat treated under the same conditions as HT LLZO. Compared to the purely water treated sample, heat treatment decreases the amount of surface carbon and reveals more LLZO; however, $La(OH)_3$ persists on the surface, and the La 3d peak separation for the WT:HT sample remains similar to the WT sample. SEM of WT:HT LLZO (Figure 3k) indicates that heat treatment does not alter the surface morphology of WT LLZO but does substantially decrease the dark patches observed on WT LLZO associated with surface carbon.

Acid Treated LLZO (AT)

Finally, Figures 3f and 3l depict XPS and SEM of polished LLZO that was immersed in 1M HCl for 45 min. The XPS results show that acid treatment is not effective for removing surface contaminants as the AT surface is dominated by LiOH and Li_2CO_3. However, unlike other surface treatments discussed thus far, acid treatment significantly alters the morphology of LLZO[32–34]—this microstructural change is further illustrated in Figure S13, which shows the continuous etching of grains and grain boundaries on the cleaved LLZO surface with prolonged acid exposure.

Characterization of Li^+/H^+ Exchange Resulting from Surface Treatments via ToF-SIMS

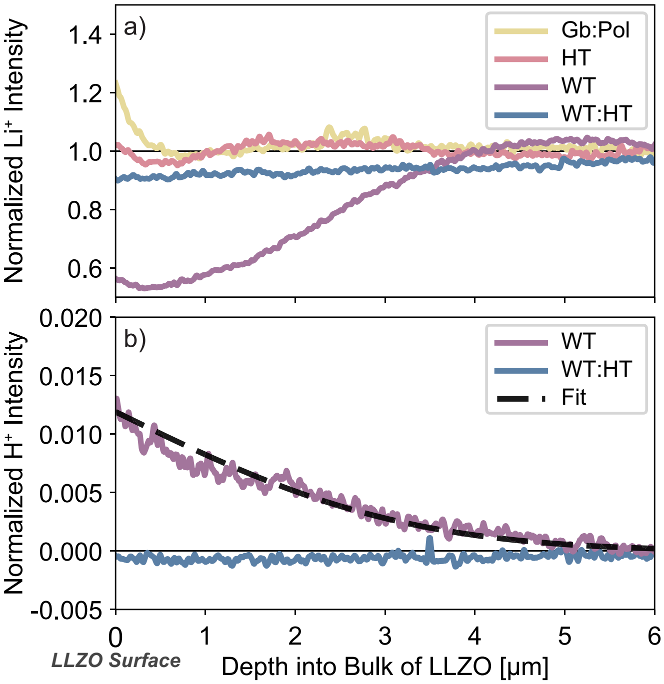

Figure 4: ToF-SIMS depth profiles from Gb:Pol, HT, WT, and WT:HT LLZO. **(a)** $^6Li^+$ intensity normalized to the bulk intensity of $^6Li^+$ in each sample; traces all converge within 12 µm (Figure S14). **(b)** H^+ intensity normalized to the bulk intensity of $^6Li^+$ alongside the result from fitting a 1D diffusion equation to the WT data. Data in (b) were standardized by subtracting the average value of the last 1 µm to set the deep-bulk H^+ levels to zero. All data are plotted such that 0 µm corresponds to the start of the LLZO bulk.

To supplement the XPS surface chemistry investigation and directly quantify the extent of Li^+ loss and H^+ insertion into LLZO as a result of surface treatments, we characterized representative samples using ToF-SIMS (measurement details in Experimental section). The extent of Li^+/H^+ exchange depends on the H^+ and Li^+ activities in the solvent. We expect non-solvent-exposed samples, such as Gb:Pol LLZO, to have the lowest extent of exchange, while WT, WT:HT, and AT LLZO samples have significant exchange due to the high H^+ activity and low Li^+ activity in the solvents used. Due to the non-uniform surface topography of LLZO post–acid exposure, AT LLZO could not be reliably characterized using ToF-SIMS.

A subset of the ToF-SIMS results are presented in Figure 4 (and additional data is presented in Figure S14). The depth profiling measurement for each sample was continued until the bulk LLZO species' concentration stabilized. Each sample had varying levels of surface contamination due to environmental exposure prior to the measurement. Therefore, to specifically compare changes to $^6Li^+$ and H^+ within the LLZO lattice, we only examine sub-surface data where contaminants do not contribute to the ToF-SIMS signal. The LaO^+ trace stabilizes quickly in each dataset and thus was used to determine when the LLZO bulk had been reached (Figure S15). All other species plateau before the measurement is concluded (final sputtered depth between 7–12 μm); therefore, average intensities were taken over the final 1 μm for each measurement to quantify the bulk intensity for each species, which was then used for normalization.

Figure 4a shows the $^6Li^+$ signal normalized by its bulk intensity; values greater than 1.0 indicate Li enrichment, and values lower than 1.0 indicate Li depletion. WT LLZO is significantly depleted of Li in the first 4 μm of LLZO, reaching a minimum of 53% of the baseline Li^+ intensity. WT:HT LLZO also exhibits Li^+ depletion but has more Li^+ near the surface than the WT sample; however, the depletion region in the WT:HT sample extends much farther into the bulk compared to the WT sample (the WT:HT Li^+ signal plateaus after 10 μm). This suggests that heat treatment facilitates Li^+ rearrangement in LLZO and that Li^+ lost in the near-surface region is supplemented by Li^+ from deeper in the bulk of the material. Gb:Pol and HT LLZO both exhibit Li^+ enrichment followed by slight Li^+ depletion near the surface; however, the magnitude of this depletion is much smaller than that of the WT and WT:HT samples, which is consistent with our hypothesis. HT LLZO displays less extreme Li fluctuations than Gb:Pol LLZO, further supporting the hypothesis that heat treatment enhances chemical diffusion and enables solute redistribution within LLZO to minimize concentration gradients. However, ToF-SIMS samples have also been shown to exhibit intensity spikes at material boundaries[50], so this initial Li^+ enrichment may be a measurement artifact.

The Li^+ depletion in WT LLZO is accompanied by H^+ enrichment in the same volume of LLZO, as seen in Figure 4b. The data in Figure 4b has been normalized to the bulk average intensity of $^6Li^+$ and subsequently standardized by subtracting the bulk average value of the normalized trace. Therefore, a value of zero indicates that the H^+ intensity is identical to that of H^+ far into the bulk of LLZO. In contrast to the WT LLZO sample, the WT:HT LLZO sample shows a flat H^+ profile—this is to be expected after heat treatment facilitated solute redistribution, since the total amount of H^+ in the lattice is negligible compared to the Li^+ concentration.

The WT LLZO H^+ profile represents the proton concentration distribution after 168 h; we fit Fick's Second Law to estimate the diffusion coefficient of H^+ in LLZO, $5 \times 10^{-18}\,\mathrm{m^2\,s^{-1}}$ (full derivation in SI). This is consistent with the recently reported chemical diffusion coefficients for H^+ in LLZO ($2\times10^{-17}\,\mathrm{m^2\,s^{-1}}$ at room temperature[56] and $7\times10^{-17}\,\mathrm{m^2\,s^{-1}}$ at $80\,^{\circ}\mathrm{C}$[57]). Furthermore, the existence of a proton concentration gradient in the bulk of WT LLZO corroborates reports that the LLZO proton exchange is diffusion-limited rather than reaction-limited[20,57], since the H^+ concentration would be constant in a purely reaction-limited scenario.

Impact of Surface Treatments on Impedance Contributions

Significant work has been done to understand and model the impedance contributions at the Li metal interface of LLZO[58–63]. Building on these findings, we examined the impacts of surface chemistry and Li^+/H^+ exchange on the electrochemical properties of LLZO via EIS using Li|LLZO|Li symmetric cells. We further validated the physical origins of different impedance contributions using pressure-varying and current-biased EIS measurements. Pressure-varying EIS is used to identify void-derived constriction, while current-biased EIS is used to differentiate ohmic impedance contributions (constriction, bulk, or grain boundary conduction) from non-ohmic contributions (e.g., charge-transfer). We discuss the interpretation of impedance contributions alongside the fitted parameters from different surface treatments.

Figures 5a-b depict the equivalent circuit model that is fit to impedance data and representative Nyquist plots obtained from HT and WT:HT LLZO cells. This circuit model considers four impedance contributions in order of decreasing characteristic frequency: 1) the bulk impedance (Z_{Bulk}) corresponding to ion migration within LLZO grains, 2) the grain boundary impedance (Z_{GB}) corresponding to ion migration within LLZO grain boundaries, 3) the interfacial impedance (Z_{Int}) which is interpreted as a constriction effect, and 4) a low-frequency impedance feature (Z_{LF}) which is attributed to an electrochemical reaction. These contributions correspond to the four peaks

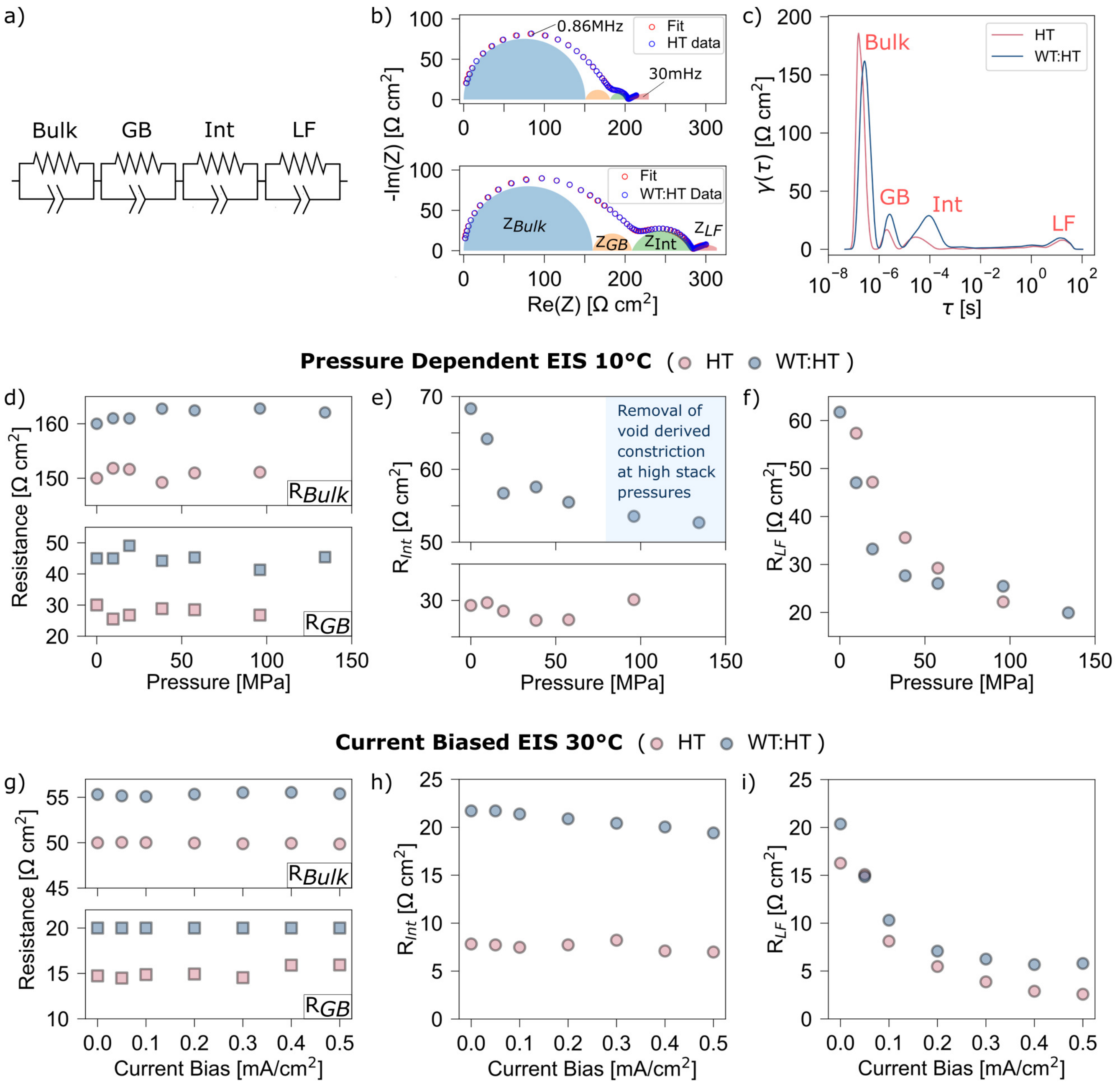

Figure 5: **(a)** Equivalent circuit that is fit to EIS data. **(b)** Nyquist plots of Li symmetric cells using HT and WT:HT LLZO measured at 10 °C. **(c)** Corresponding DRT analysis on impedance data shown in **(b)** illustrating 4 impedance contributions. The HT and WT:HT cells shown in **(b)** and **(c)** are subjected to current-biased EIS measurements to delineate ohmic vs. non-ohmic features; subsequent pressure-dependent EIS measurements on the same cells assess the presence of voids. Figures **(d)-(f)** depict fitted bulk, grain boundary, interfacial, and low-frequency resistance contributions from pressure-dependent EIS measurements at 10 °C; the pressure was increased until electrolyte fracture and short circuiting occurred. Figures **(g)-(i)** depict fitted bulk, grain boundary, interfacial, and low-frequency resistance contributions from current-biased EIS measurements at 30 °C.

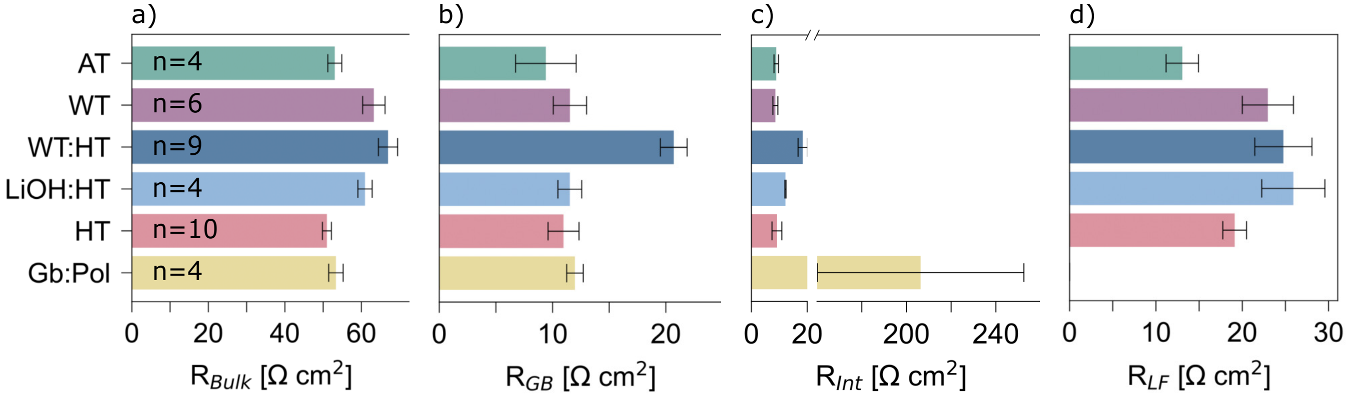

Figure 6: Extracted **(a)** bulk, **(b)** grain boundary **(c)** interfacial, and **(d)** low-frequency resistances from EIS measurements of Li|LLZO|Li symmetric cells after different surface treatments. All EIS measurements were made at 30 °C. Error bars represent the standard error for each surface treatment computed from $n \geq 4$ replicates. R_{LF} for Gb:Pol LLZO in **(d)** is not fitted due to being convoluted with R_{Int}—tall voids or large constriction resistances are known to reduce the characteristic frequency of constriction impedance[58].

identified from the DRT[51] analysis shown in Figure 5c.

Z_{Bulk}

Figures 5d and 5g show that R_{Bulk} remains invariant under pressure-dependent and current-biased EIS measurements, consistent with an ohmic impedance feature not associated with interfacial contact. Li^+/H^+ exchange is expected to decrease the bulk ionic conductivity as a result of the low self-diffusivity of H^+[64] in comparison to Li^+[65] in LLZO. Indeed, these trends are reflected by fitted R_{Bulk} values shown in Figure 6a. Water exposure induces the greatest amount of Li^+/H^+ exchange and results in the most substantial increase in R_{Bulk} compared to non-solvent-exposed samples (Gb:Pol and HT LLZO). The similarity of R_{Bulk} between WT and WT:HT samples signifies that decreases in bulk conductivity cannot be solely attributed to Li^+ deficient surface layers, such as those observed in WT LLZO. Equalization of Li^+/H^+ concentration gradients after heat treatment in WT:HT LLZO does not decrease R_{Bulk}, suggesting that ionic conductivity in LLZO is more affected by the extent of H^+ exchange instead of the distribution of H^+.

Similar to previous reports, using an aqueous 3M LiOH solution lessens the increase in R_{Bulk}[11,12], indicating that the Li^+ and H^+ activity of a solution alters the extent of proton exchange. Interestingly, acid treatment results in smaller increases to R_{Bulk} compared to water-exposed samples (WT, WT:HT, and LiOH:HT LLZO). We postulate that this occurs due to Li metal infiltration into the porous microstructure of the acid treated samples—increases to the Li electrode area and decreases to the vertical electrode separation can offset conductivity losses from proton exchange.

$\mathbf{Z}_{GB}$

Similar to Z_{Bulk}, Z_{GB} remains invariant under pressure-dependent and current-biased EIS measurements, which is consistent with an ohmic impedance feature not associated with interfacial contact. Data in Figure 6b show that R_{GB} does not vary across different surface treatments with the exception of WT:HT LLZO, which possesses an average R_{GB} that is double that of the other sample types. Notably, this elevated grain boundary resistance only occurs after annealing the WT sample. ToF-SIMS data presented in Figure 4a shows that heat treatment removes the surface Li^+ depletion region in WT LLZO, thus indicating a redistribution of H^+ away from the surface. We speculate that heat treatment facilitates H^+ segregation to LLZO grain boundaries or that the grain boundary conductivity is highly sensitive to protonation.

$\mathbf{Z}_{Int}$

Figure 6c shows the effect of surface treatments on R_{Int}, which we interpret as a constriction impedance at the Li|LLZO interface. R_{Int} is highest for samples that are heavily contaminated with LiOH or Li_2CO_3 (e.g., Gb:Pol LLZO). Removal of lithiophobic LiOH/Li_2CO_3 through water treatment or heat treatment substantially decreases R_{Int}, consistent with R_{Int} being largely dictated by Li wetting at the LLZO interface[24]. An exception to this is AT LLZO—Li infiltration into the porous microstructure enables significantly improved lateral contact despite substantial surface contamination. It is worth emphasizing that constriction resistance, which arises from distortions to electric field lines, is caused by purely geometric effects, such as inhomogeneous contact at the Li|LLZO interface[29,58,63]. Current-biased galvanostatic EIS measurements shown in Figure 5h demonstrate the ohmic nature of R_{Int}, indicating that R_{Int} is unlikely to be associated with a charge-transfer process.

We further investigate the physical origin of Z_{Int} using pressure-dependent EIS measurements. Figure 5e shows that R_{Int} values for WT:HT LLZO decrease with increasing stack pressure until approximately 100 MPa, after which they plateau; for HT LLZO, R_{Int} remains near-constant at around $30\,\Omega\,cm^2$. Voids at the Li|LLZO interface should, in principle, be completely removed by high stack pressures[60]. However, the plateauing of R_{Int} at values significantly greater than 0, even at stack pressures close to electrolyte fracture, indicates that void-derived constriction may not be the only contribution to Z_{Int}. We postulate that an additional component of R_{Int} arises from ionically-resistive interlayers at the Li|LLZO interface. This interpretation is consistent with our XPS results, which demonstrate that ionically-resistive species, such as LiOH, are almost impossible to avoid on LLZO surfaces. These species are also likely to be present on Li metal electrodes[66,67].

$\mathbf{Z}_{LF}$

Finally, we observe a low-frequency impedance response with a characteristic frequency on the order of 10^{-2}–10^{-3} Hz across all Li symmetric cells that possess low R_{Int} values. Fitted R_{LF} values from current-biased EIS measurements (Figure 5i) confirm that R_{LF} is non-ohmic; the decrease in R_{LF} with increasing biasing current is consistent with a charge-transfer reaction. This trend holds for both positive and negative current-biasing directions (Figure S23). Previous studies have attributed Z_{LF} to an electrochemical reaction[60,61,68,69]; in particular, the inverse relation between R_{LF} and pressure (Figure 5f) has been highlighted by Wang and coworkers, who associate the kinetics with vacancy or adatom motion of Li[61]. Further work is being done to understand why Z_{LF} occurs at such low characteristic frequencies, and the nature of the associated capacitance, if it is a charge-transfer process.

Modeling Constriction at the Li Metal Interface

Based on our pressure-dependent EIS measurements, we postulate that SSB constriction impedance, attributed to Z_{Int} in our impedance data, arises from a combination of voids and ionically-resistive surface layers. To better understand the different factors impacting constriction at the Li|LLZO interface, we modeled the impedance response of SSBs under different geometric configurations by performing FEM calculations based off work by Fleig and coworkers[29]. Additionally, we explored the connection between constriction impedance and ionic conductivity to clarify the detrimental impact of Li^+/H^+ exchange on LLZO constriction. Figure 7 illustrates the four distinct cases considered. This model only considers bulk ion migration in the absence of any Faradaic redox reactions or concentration gradients (model details are provided in the SI).

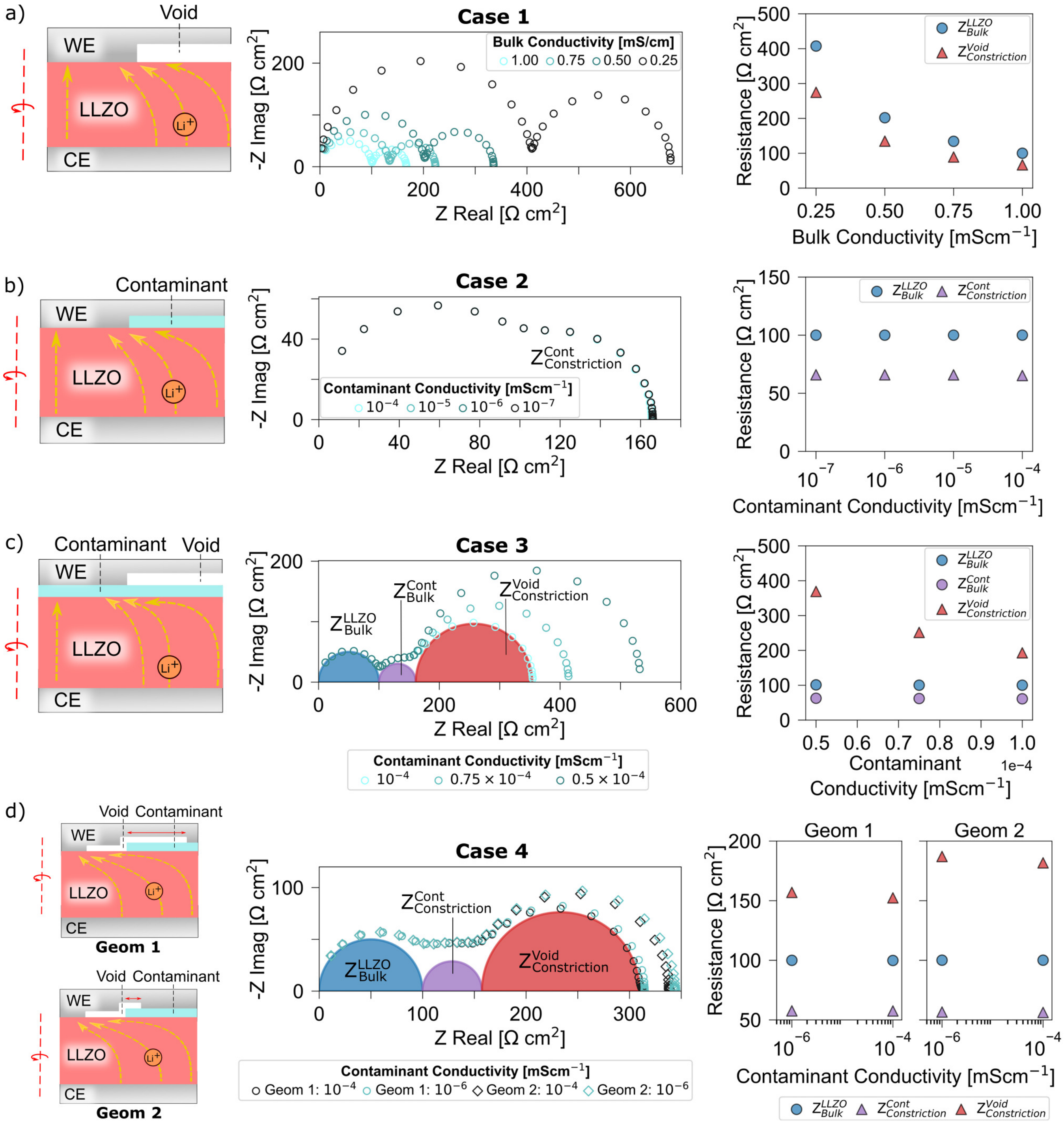

Figure 7: Simulated impedance data from FEM calculations that illustrate how conductivity impacts constriction impedance at the Li|LLZO interface under different geometries: **(a)** effect of electrolyte conductivity on void-derived constriction; **(b)** effect of contaminant conductivity on contaminant-derived constriction; **(c)** effect of contaminant conductivity on void-derived constriction atop a uniform contaminant layer; **(d)** effect of contaminant conductivity when both void-derived constriction and contaminant-derived constriction coexist. Each Nyquist plot is accompanied by the corresponding FEM model geometry on the left and resistance plots on the right from equivalent circuit fitting. For each annotated impedance feature, the subscript denotes the physical process (e.g., constriction), while the superscript denotes the source (e.g., voids).

Cases 1 and 2 demonstrate that the presence of a 10 µm thick void or contaminant layer can give rise to a constriction impedance that is distinct from Z_{Bulk}. In both cases, the constriction feature arises due to an interfacial region with different dielectric properties and substantially lower ionic conductivity than the bulk electrolyte. At high frequencies, current can flow through the voids or contaminants via the displacement current, thus giving a Z_{Bulk} response identical to electrodes with uniform contact. At low frequencies, the poor conductivity of voids or contaminants restricts current flow to regions with Li|SE contact. As discussed in previous works[29,58,60,63], the characteristic frequency of constriction impedance at Li metal interfaces is dependent on the geometry and dielectric constant of the void or contaminant layer; resistive layers with high thickness and low surface area increase the characteristic frequency of the constriction impedance, potentially rendering it indistinguishable from Z_{Bulk}. Furthermore, the real Li|SE interface likely possesses a distribution of void or contaminant geometries. Nonetheless, our model demonstrates that both voids and contaminants with micron-scale thickness are capable of generating a distinct constriction feature in EIS measurements.

Current constriction arises from deviations to the conduction pathway; thus, the conductivity of this pathway will influence the magnitude of the constriction resistance. The Nyquist plots shown in Figure 7a demonstrate how decreases in the electrolyte conductivity result in proportional increases to both R_{Bulk} and constriction resistance. Therefore, solid electrolytes with lower ionic conductivities (e.g., protonated LLZO) will have higher constriction resistances, assuming a similar Li contact geometry is maintained. This correlation is illustrated in Figure S27 for HT, LiOH:HT, and WT:HT LLZO, which are expected to have distinct protonation levels.

The effect of conductivity extends to any element of the conduction pathway but is most pronounced for components conducting the majority of charge. Case 2, where constriction comes purely from contaminants, demonstrates this phenomenon—constriction impedance is practically unaffected by the contaminant conductivity because the majority of the current bypasses the contaminant layer. This is contrasted in Case 3, where current must pass through a uniform contaminant layer; in this scenario, contaminant conductivity strongly affects the constriction impedance. Both Case 2 and 3 refer to contaminants, but these results apply for any ionically-resistive layer (e.g., H^+ exchanged

LLZO or artificial coatings on solid electrolytes).

In real systems, contaminant coverage on LLZO can be non-uniform and constriction due to both voids and ionically-resistive layers can coexist. Two such geometries are schematically shown in Case 4 (Figure 7d), which depicts voids of different areas partially covering both the solid electrolyte and contaminant. As in Case 2, varying contaminant conductivity (even by 2 orders of magnitude) barely affects constriction because only a small portion of the current passes through the contaminant layer. For the same reason, altering the void coverage on top of the contaminant (Geom 1 vs. Geom 2) has little effect, since this only affects the void-derived constriction in series with the contaminant layer. In the DC (low-frequency) limit, current constriction already occurs via components of the void and contaminant layer directly in contact with the solid electrolyte. Therefore, the addition of voids on top of a resistive layer does not strongly alter the constriction resistance unless a substantial fraction of the total current passes through the resistive layer (as in Case 3). For LLZO surfaces without uniform contaminant coverage, constriction impedance may be dictated by properties of the contaminant layer, rather than voids, despite poor Li wetting on the contaminant layer.

Overpotential-Induced Open Circuit Failure During Cell Cycling

To elucidate the functional impact of LLZO surface chemistry, especially the effect on unstable overpotential growth, we performed galvanostatic cycling on 37 Li|LLZO|Li symmetric cells using pellets prepared via the surface treatments discussed thus far. We used a standardized cycling protocol that included five initial low-current formation cycles at $0.01\,\mathrm{mA\,cm^{-2}}$, one cycle at $0.05\,\mathrm{mA\,cm^{-2}}$, and then three cycles at higher current densities that were sequentially increased by $0.05\,\mathrm{mA\,cm^{-2}}$ intervals until cell failure. Apart from the formation cycles, each half-cycle had a constant capacity of $1\,\mathrm{mAh\,cm^{-2}}$. The impedance was measured five times after each half-cycle to monitor cell degradation. The relatively large half-cycle capacity and repeated cycles were chosen to test the overpotential stability at each current density. A representative cycling curve for a HT LLZO sample is shown in Figure 8a (see Figure S30 for the full-range voltage plot). Here, unstable overpotential growth is visible in the voltage trace beginning at $0.2\,\mathrm{mA\,cm^{-2}}$ (4.2×10^5 s).

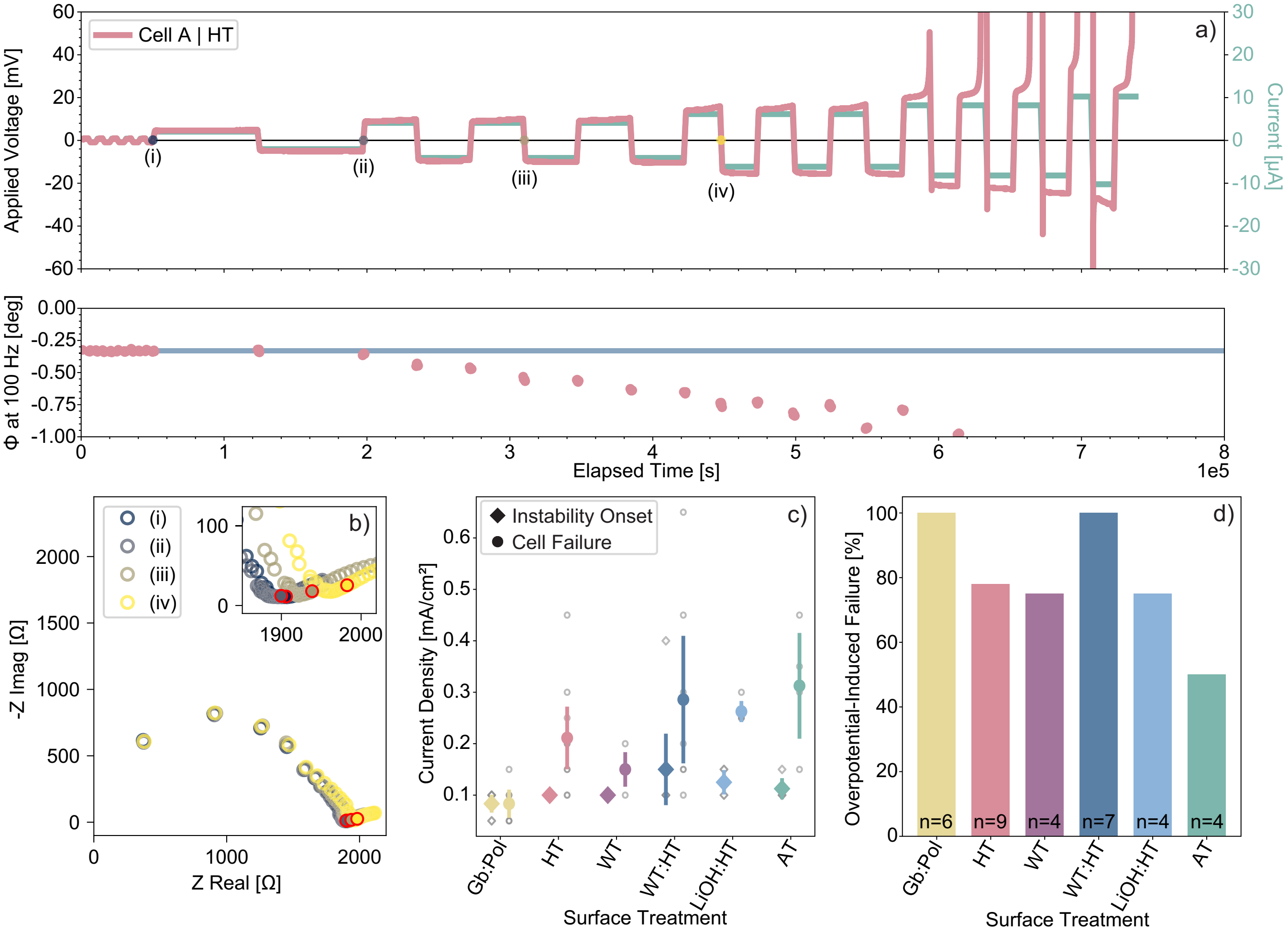

Figure 8: Cell cycling results on Li|LLZO|Li cells cycled under 10 MPa stack pressure at 30 °C. **(a)** The upper plot is a representative voltage vs. time trace for a HT LLZO cell (Cell A); current vs. time is shown on the secondary y-axis. The lower plot shows the phase of the impedance (Φ) at 100 Hz from EIS spectra taken between half-cycles. The blue shaded band marks the initial average phase $\pm 3\sigma$. **(b)** Mid-cycling EIS spectra for Cell A with data from 100 Hz marked by red outlines; time points for each EIS spectra are marked in (a). **(c)** Scatter plot showing the mean current density at the onset of unstable overpotential growth (diamonds) and at failure (circles) separated by treatment; vertical lines indicate the 90% confidence interval of the mean, and individual cell data is shown in gray. **(d)** Percentage of cells that failed via overpotential-induced failure as a function of surface treatment.

Figure 8d shows that only 7 of the 37 cycled cells failed by short-circuiting; instead, most experiments stopped due to excessive overpotential buildup that exceeded the ±10 V compliance limit of the cell cycling electronics. Furthermore, even the cells that short-circuited exhibited overpotentials above 1 V prior to failure. As discussed in the previous section, this overpotential buildup is likely the result of constriction resistance from voids or contaminants at the Li|LLZO interface. Therefore, cell performance in this study is characterized by (i) the current density at which the overpotential begins growing unstably and (ii) the current density at cell failure due to excessive overpotential buildup or short-circuiting. Short-circuiting in symmetric SSBs has an unambiguous electrical signature that is ubiquitously used for finding critical current density; however, there currently is no established electrical signal for indicating the onset of unstable overpotential buildup.

Overpotential instability is most often determined based on arbitrary voltage-related criteria, but we have found that the impedance behavior is a more sensitive indicator of unstable overpotential growth. Specifically, the phase of the impedance, Φ, (and the imaginary component of the impedance) registers instability earlier, and more accurately, than the applied voltage while cycling. Part of this sensitivity can be attributed to the higher dynamic range used by the control electronics during impedance measurements, but the accuracy of the phase criteria stems from how Φ relates to the actual cell behavior. The FEM results above (and previous studies[58,63]) show that void- and contaminant-derived current constriction appears at lower frequencies in EIS spectra; correspondingly, Φ decreases at lower frequencies as a cell becomes more unstable and the interface devolves. For example, the lower plot in Figure 8a shows Φ at 100 Hz (taken from the post-half-cycle impedance spectra); the horizontal blue band demarcates the initial average phase $\pm 3\sigma$. Figure 8b plots select EIS spectra from Cell A at four time points to demonstrate the impedance evolution during cycling (and 100 Hz is indicated by the red circles). A perfectly stable cell should have an invariant impedance magnitude and phase, but Φ deviating beyond the marked range indicates that statistically-significant overpotential instability has occurred within the cell. In Figure 8a, unstable overpotential growth begins at around 2×10^5 s based on this phase criterion; however, even a strict voltage criterion (e.g., $\geq 10\%$ change in overpotential within a half-cycle) does not register instability until 3×10^5 s, and tighter voltage limits are not possible due to measurement noise. The SI contains further explanation and Φ evolution for all frequencies.

Cell performance data in Figure 8c shows that a higher onset current density for unstable overpotential growth does not directly imply a higher current density for cell failure. This is highlighted for AT samples, which, despite possessing the highest average current density for failure, exhibit overpotential instability at a lower current density compared to WT:HT and LiOH:HT samples. AT LLZO is able to sustain higher nominal current densities before failure due to the porous surface morphology that increases the effective Li|LLZO contact area[32–34]. However, the AT surface is contaminated by Li_2CO_3 and LiOH—these lithiophobic species lead to current constriction, which manifests as overpotential instability at lower current densities.

Several distinct patterns emerge by incorporating insights from the earlier surface chemistry and Li^+ /H^+ exchange characterization. First, the onset of unstable overpotential growth trends higher for samples with less contaminated surfaces (HT LLZO vs. Gb:Pol LLZO and WT:HT LLZO vs. WT LLZO)—these cells likely experience primarily void-derived constriction with fewer contaminant-derived impacts. Second, all samples exposed to water (WT, WT:HT and LiOH:HT) have equal or greater average current densities for unstable overpotential growth compared to Gb:Pol and HT LLZO. This may be linked to $La(OH)_3$ which exists on all samples exposed to water; however, further investigation is needed to confirm the effect of $La(OH)_3$ on Li wetting and interfacial stability. Third, cells that were heat treated survive until much higher current densities than their non–heat treated counterparts. Specifically, the WT vs. WT:HT results suggest that the heterogeneous distribution of H^+ in WT LLZO may be more detrimental than the extent of Li^+ /H^+ exchange, which should be the same for both sample types.

Finally, cycling performance has no clear correlation to the pre-cycling EIS parameters from Figure 6. For instance, R_{Int} does not appear to be a strong predictor of cell longevity (Figure S32c) unless it is significantly higher than R_{Bulk}, as is the case with Gb:Pol LLZO (Figure S32e). However, the cells with the highest R_{Int} (Gb:Pol, WT:HT) are more prone to failing via excessive overpotential buildup instead of short-circuiting. The SI contains correlation plots for the additional EIS parameters.

Conclusion

In this study, we used a combination of surface chemical analysis, modeling, and electrochemical characterization to systematically investigate the impacts of proton exchange and surface contamination reactions on LLZO solid electrolytes. Our findings demonstrate that LLZO is extremely susceptible to Li^+/H^+ exchange, so maintaining a contaminant-free surface is likely only possible above contaminant removal temperatures or under ultra-high vacuum. Li^+/H^+ exchange lowers electrolyte ionic conductivity and is limited by chemical diffusion of H^+ into the bulk electrolyte. Concentration gradients induced by Li^+/H^+ exchange in water are dissipated by heat treatment, but the bulk electrolyte conductivity is unaffected. This indicates that conductivity losses stem from the overall extent of Li^+/H^+ exchange rather than surface Li^+ depletion layers. The increase in grain boundary resistance after heat treatment also suggests that equalization of concentration gradients is accompanied by H^+ segregation to grain boundaries. Surface contaminants, such as LiOH and Li_2CO_3, introduce significant constriction resistances and lead to unstable cycling, but both contaminants can be effectively removed via heat treatment in O_2 without affecting the bulk electrolyte conductivity. NAP-XPS results show that the onset temperature for contaminant removal occurs between 350–400 °C, but a contaminant-free surface is fundamentally limited by the high moisture sensitivity of LLZO.

To supplement surface characterization and electrochemical measurements, we modeled the different impedance contributions at the Li|LLZO interface. We show that constriction is not only the result of voids between Li and LLZO but can also arise due to ionically-resistive surface layers. Furthermore, our model emphasizes the interplay between ionic conductivity and constriction. SSBs with low-conductivity components will experience higher constriction resistances, even with identical contact geometries; this motivates more careful consideration of electrolyte surfaces, including both contaminants and engineered coatings.

Finally, we highlight the importance of unstable overpotential growth as a failure mechanism that fundamentally limits practical operating current densities for Li metal SSBs. Rapid overpotential buildup without short circuiting is the dominant failure mechanism for Li symmetric cells operated at moderate half cycle capacities of $1\,\mathrm{mAh\,cm^{-2}}$; even for cells that short-circuit, non-catastrophic overpotential accumulation precedes dendritic failure. Notably, fluctuations in the phase angle of the impedance response in symmetric cells serve as a highly sensitive and accurate indicator for the onset of unstable overpotential growth. Overall, this work advances the understanding of surface contamination reactions on LLZO and establishes correlative insights into electrochemical performance that are broadly applicable to other solid electrolyte systems.

Acknowledgement

This work was supported by the Samsung Advanced Institute of Technology. Some characterization aspects of the work were supported by the Assistant Secretary for Energy Efficiency, Vehicle Technologies Office of the US Department of Energy under the Advanced Battery Materials Research Program. This research used resources of the Advanced Light Source, which is a DOE Office of Science User Facility under contract no. DE-AC02-05CH11231. Part of this work was performed at the Stanford Nano Shared Facilities, supported by the National Science Foundation under award ECCS-2026822. S.W. acknowledges support from the Quad Fellowship. E.B. acknowledges support by a National Science Foundation Graduate Fellowship. We thank Emma Kaeli, Tony Dong, and Nicholas Liang for their helpful discussions and comments on the manuscript.

Supporting Information Available

Supporting Information: Additional characterization data, alternative visualizations, explanations for data treatment, and derivations for equations referenced in the main text.

References

(1) Albertus, P.; Babinec, S.; Litzelman, S.; Newman, A. Status and challenges in enabling the lithium metal electrode for high-energy and low-cost rechargeable batteries. *Nature Energy* **2018**, *3*, 16–21.

(2) Liu, J. et al. Pathways for practical high-energy long-cycling lithium metal batteries. *Nature Energy* **2019**, *4*, 180–186.

(3) Inoue, T.; Mukai, K. Are all-solid-state lithium-ion batteries really safe?-verification by differential scanning calorimetry with an all-inclusive microcell. *ACS Applied Materials and Interfaces* **2017**, *9*, 1507–1515.

(4) Manthiram, A.; Yu, X.; Wang, S. Lithium battery chemistries enabled by solid-state electrolytes. *Nature Reviews Materials* **2017**, *2*, 1–16.

(5) Famprikis, T.; Canepa, P.; Dawson, J. A.; Islam, M. S.; Masquelier, C. Fundamentals of inorganic solid-state electrolytes for batteries. *Nature Materials* **2019**, *18*, 1278–1291.

(6) Janek, J.; Zeier, W. G. A solid future for battery development. 2016.

(7) Nakayama, M.; Kotobuki, M.; Munakata, H.; Nogami, M.; Kanamura, K. First-principles density functional calculation of electrochemical stability of fast Li ion conducting garnet-type oxides. *Physical Chemistry Chemical Physics* **2012**, *14*, 10008–10014.

(8) Krauskopf, T.; Richter, F. H.; Zeier, W. G.; Janek, J. Physicochemical Concepts of the Lithium Metal Anode in Solid-State Batteries. *Chemical Reviews* **2020**, *120*, 7745–7794.

(9) Hofstetter, K.; Samson, A. J.; Narayanan, S.; Thangadurai, V. Present understanding of the stability of Li-stuffed garnets with moisture, carbon dioxide, and metallic lithium. *Journal of Power Sources* **2018**, *390*, 297–312.

(10) Zhu, Y.; Connell, J. G.; Tepavcevic, S.; Zapol, P.; Garcia-Mendez, R.; Taylor, N. J.; Sakamoto, J.; Ingram, B. J.; Curtiss, L. A.; Freeland, J. W.; Fong, D. D.; Markovic, N. M. Dopant-Dependent Stability of Garnet Solid Electrolyte Interfaces with Lithium Metal. *Advanced Energy Materials* **2019**, *9*, 1803440.

(11) Shimonishi, Y.; Toda, A.; Zhang, T.; Hirano, A.; Imanishi, N.; Yamamoto, O.; Takeda, Y. Synthesis of garnet-type Li7 - XLa3Zr 2O12 - 1/2x and its stability in aqueous solutions. *Solid State Ionics* **2011**, *183*, 48–53.

(12) Yow, Z. F.; Oh, Y. L.; Gu, W.; Rao, R. P.; Adams, S. Effect of Li+/H+ exchange in water treated Ta-doped Li7La3Zr2O12. *Solid State Ionics* **2016**, *292*, 122–129.

(13) Galven, C.; Dittmer, J.; Suard, E.; Le Berre, F.; Crosnier-Lopez, M. P. Instability of lithium garnets against moisture. Structural characterization and dynamics of Li 7-xH xLa 3Sn 2O 12 and Li 5-xH xLa 3Nb 2O 12. *Chemistry of Materials* **2012**, *24*, 3335–3345.

(14) Jin, Y.; McGinn, P. J. Li7La3Zr2O12 electrolyte stability in air and fabrication of a Li/Li7La3Zr 2O12/Cu0.1V2O5 solid-state battery. *Journal of Power Sources* **2013**, *239*, 326–331.

(15) Cheng, M.; Rangasamy, E.; Liang, C.; Sakamoto, J.; More, K. L.; Chi, M. Excellent stability of a lithium-ion-conducting solid electrolyte upon reversible LI+/H+ exchange in aqueous solutions. *Angewandte Chemie - International Edition* **2015**, *54*, 129–133.

(16) Orera, A.; Larraz, G.; Rodríguez-Velamazán, J. A.; Campo, J.; Sanjuán, M. L. Influence of Li+ and H+ Distribution on the Crystal Structure of Li7-xHxLa3Zr2O12 (0 = ≤ x ≤ = 5) Garnets. *Inorganic Chemistry* **2016**, *55*, 1324–1332.

(17) Xia, W.; Xu, B.; Duan, H.; Tang, X.; Guo, Y.; Kang, H.; Li, H.; Liu, H. Reaction mechanisms of lithium garnet pellets in ambient air: The effect of humidity and CO2. *Journal of the American Ceramic Society* **2017**, *100*, 2832–2839.

(18) Brugge, R. H.; Hekselman, A. K.; Cavallaro, A.; Pesci, F. M.; Chater, R. J.; Kilner, J. A.; Aguadero, A. Garnet Electrolytes for Solid State Batteries: Visualization of Moisture-Induced Chemical Degradation and Revealing Its Impact on the Li-Ion Dynamics. *Chemistry of Materials* **2018**, *30*, 3704–3713.

(19) Liu, X.; Chen, Y.; Hood, Z. D.; Ma, C.; Yu, S.; Sharafi, A.; Wang, H.; An, K.; Sakamoto, J.; Siegel, D. J.; Cheng, Y.; Jalarvo, N. H.; Chi, M. Elucidating the mobility of H+ and Li+ ions in (Li6.25-: XHxAl0.25)La3Zr2O12 via correlative neutron and electron spectroscopy. *Energy and Environmental Science* **2019**, *12*, 945–951.

(20) Redhammer, G. J.; Badami, P.; Meven, M.; Ganschow, S.; Berendts, S.; Tippelt, G.; Rettenwander, D. Wet-Environment-Induced Structural Alterations in Single- And Polycrystalline LLZTO Solid Electrolytes Studied by Diffraction Techniques. *ACS Applied Materials and Interfaces* **2021**, *13*, 350–359.

(21) Arinicheva, Y.; Guo, X.; Gerhards, M. T.; Tietz, F.; Fattakhova-Rohlfing, D.; Finsterbusch, M.; Navrotsky, A.; Guillon, O. Competing Effects in the Hydration Mechanism of a Garnet-Type Li7La3Zr2O12 Electrolyte. *Chemistry of Materials* **2022**, *34*, 1473–1480.

(22) La, L.; Ta, Z.; Electrolyte, O. S.; Air, A.; Hoinkis, N.; Schuhmacher, J.; Leukel, S.; Loho, C.; Roters, A.; Richter, F. H.; Janek, J. Particle Size-Dependent Degradation Kinetics of Garnet-Type. **2023**,

(23) Nakayama, M.; Horie, T.; Natsume, R.; Hashimura, S.; Tanibata, N.; Takeda, H.; Maeda, H.; Kotobuki, M. Reaction Kinetics of Carbonation at the Surface of Garnet-Type Li 7 La 3 Zr 2 O 12 as Solid Electrolytes for All-Solid-State Li Ion Batteries. **2023**, 3–9.

(24) Sharafi, A.; Kazyak, E.; Davis, A. L.; Yu, S.; Thompson, T.; Siegel, D. J.; Dasgupta, N. P.; Sakamoto, J. Surface Chemistry Mechanism of Ultra-Low Interfacial Resistance in the Solid-State Electrolyte Li7La3Zr2O12. *Chemistry of Materials* **2017**, *29*, 7961–7968.

(25) Sharafi, A.; Yu, S.; Naguib, M.; Lee, M.; Ma, C.; Meyer, H. M.; Nanda, J.; Chi, M.; Siegel, D. J.; Sakamoto, J. Impact of air exposure and surface chemistry on Li-Li7La3Zr2O12 interfacial resistance. *Journal of Materials Chemistry A* **2017**, *5*, 13475–13487.

(26) Krauskopf, T. a. F. U. o. t. L. M. A. i. S.-S. B. A. E.-M. S. o. t. G.-T. S. E. L. . A. . L.; Hartmann, H.; Zeier, W. G.; Janek, J. Toward a Fundamental Understanding of the Lithium Metal Anode in Solid-State Batteries - An Electrochemo-Mechanical Study on the Garnet-Type Solid Electrolyte Li 6.25 Al 0.25 La 3 Zr 2 O 12. *ACS Applied Materials and Interfaces* **2019**, *11*, 14463–14477.

(27) Krauskopf, T.; Mogwitz, B.; Rosenbach, C.; Zeier, W. G.; Janek, J. Diffusion Limitation of Lithium Metal and Li–Mg Alloy Anodes on LLZO Type Solid Electrolytes as a Function of Temperature and Pressure. *Advanced Energy Materials* **2019**, *9*.

(28) Grissa, R.; Payandeh, S.; Heinz, M.; Battaglia, C. Impact of Protonation on the Electrochemical Performance of Li 7 La 3 Zr 2 O 12 Garnets . *ACS Applied Materials & Interfaces* **2021**,

(29) Fleig, J.; Maier, J. The Influence of Laterally Inhomogeneous Contacts on the Impedance of Solid Materials: A Three-Dimensional Finite-Element Study. *Journal of Electroceramics* **1997**, *1*, 73–89.

(30) Cheng, L.; Liu, M.; Mehta, A.; Xin, H.; Lin, F.; Persson, K.; Chen, G.; Crumlin, E. J.; Doeff, M. Garnet Electrolyte Surface Degradation and Recovery. *ACS Applied Energy Materials* **2018**, *1*, 7244–7252.

(31) Vema, S.; Sayed, F.; Nagendran, S.; Karagoz, B.; Paulus, M.; Sternemann, C.; Held, G.; Grey, C. Understanding the surface regeneration and reactivity of garnet solid electrolytes. *ACS Energy Letters* **2023**,

(32) Huo, H.; Chen, Y.; Zhao, N.; Lin, X.; Luo, J.; Yang, X.; Liu, Y.; Guo, X.; Sun, X. In-situ formed Li2CO3-free garnet/Li interface by rapid acid treatment for dendrite-free solid-state batteries. *Nano Energy* **2019**, *61*, 119–125.

(33) Motoyama, M.; Tanaka, Y.; Yamamoto, T.; Tsuchimine, N.; Kobayashi, S.; Iriyama, Y. The Active Interface of Ta-Doped Li7La3Zr2O12 for Li Plating/Stripping Revealed by Acid Aqueous Etching. *ACS Applied Energy Materials* **2019**, *2*, 6720–6731.

(34) Kim, S. et al. High-energy and durable lithium metal batteries using garnet-type solid electrolytes with tailored lithium-metal compatibility. *Nature Communications* **2022**, *13*.

(35) Grissa, R.; Seidl, L.; Dachraoui, W.; Sauter, U.; Battaglia, C. Li 7 La 3 Zr 2 O 12 Protonation as a Means to Generate Porous/Dense/Porous-Structured Electrolytes for All-Solid-State Lithium-Metal Batteries. *ACS Applied Materials & Interfaces* **2022**, *296*, 1042–1045.

(36) Jonson, R. A.; McGinn, P. J. Tape casting and sintering of Li7La3Zr1.75Nb0.25Al0.1O12 with Li3BO3 additions. *Solid State Ionics* **2018**, *323*, 49–55.

(37) Yang, C.; Zhang, L.; Liu, B.; Xu, S.; Hamann, T.; McOwen, D.; Dai, J.; Luo, W.; Gong, Y.; Wachsman, E. D.; Hu, L. Continuous plating/stripping behavior of solid-state lithium metal anode in a 3D ion-conductive framework. *Proceedings of the National Academy of Sciences of the United States of America* **2018**, *115*, 3770–3775.

(38) Jonson, R. A.; Yi, E.; Shen, F.; Tucker, M. C. Optimization of Tape Casting for Fabrication of Li6.25Al0.25La3Zr2O12Sheets. *Energy and Fuels* **2021**, *35*, 8982–8990.

(39) Shen, H.; Yi, E.; Amores, M.; Cheng, L.; Tamura, N.; Parkinson, D. Y.; Chen, G.; Chen, K.; Doeff, M. Oriented porous LLZO 3D structures obtained by freeze casting for battery applications. *Journal of Materials Chemistry A* **2019**, *7*, 20861–20870.

(40) Lewis, J. A.; Lee, C.; Liu, Y.; Han, S. Y.; Prakash, D.; Klein, E. J.; Lee, H.-W.; McDowell, M. T. Role of areal capacity in determining short circuiting of sulfide-based solid-state batteries. *ACS applied materials & interfaces* **2022**, *14*, 4051–4060.

(41) Klimpel, M.; Zhang, H.; Kovalenko, M. V.; Kravchyk, K. V. Standardizing critical current density measurements in lithium garnets. *Communications Chemistry* **2023**, *6*, 192.

(42) Fuchs, T.; Haslam, C. G.; Richter, F. H.; Sakamoto, J.; Janek, J. Evaluating the use of critical current density tests of symmetric lithium transference cells with solid electrolytes. *Advanced Energy Materials* **2023**, *13*, 2302383.

(43) Koshikawa, H.; Matsuda, S.; Kamiya, K.; Miyayama, M.; Kubo, Y.; Uosaki, K.; Hashimoto, K.; Nakanishi, S. Dynamic changes in charge-transfer resistance at Li metal/Li7La3Zr2O12 interfaces during electrochemical Li dissolution/deposition cycles. *Journal of power sources* **2018**, *376*, 147–151.

(44) Kasemchainan, J.; Zekoll, S.; Spencer Jolly, D.; Ning, Z.; Hartley, G. O.; Marrow, J.; Bruce, P. G. Critical stripping current leads to dendrite formation on plating in lithium anode solid electrolyte cells. *Nature materials* **2019**, *18*, 1105–1111.

(45) Lewis, J. A.; Cortes, F. J. Q.; Liu, Y.; Miers, J. C.; Verma, A.; Vishnugopi, B. S.; Tippens, J.; Prakash, D.; Marchese, T. S.; Han, S. Y.; others Linking void and interphase evolution to electrochemistry in solid-state batteries using operando X-ray tomography. *Nature Materials* **2021**, *20*, 503–510.

(46) Ohno, S.; Bernges, T.; Buchheim, J.; Duchardt, M.; Hatz, A.-K.; Kraft, M. A.; Kwak, H.; Santhosha, A. L.; Liu, Z.; Minafra, N.; others How certain are the reported ionic conductivi-

ties of thiophosphate-based solid electrolytes? An interlaboratory study. *ACS Energy Letters* **2020**, *5*, 910–915.

(47) Fairley, N.; Fernandez, V.; Richard-Plouet, M.; Guillot-Deudon, C.; Walton, J.; Smith, E.; Flahaut, D.; Greiner, M.; Biesinger, M.; Tougaard, S.; others Systematic and collaborative approach to problem solving using X-ray photoelectron spectroscopy. *Applied Surface Science Advances* **2021**, *5*, 100112.

(48) Greczynski, G.; Hultman, L. C 1s Peak of Adventitious Carbon Aligns to the Vacuum Level: Dire Consequences for Material's Bonding Assignment by Photoelectron Spectroscopy. *ChemPhysChem* **2017**, *18*, 1507–1512.

(49) Biesinger, M. C. Accessing the robustness of adventitious carbon for charge referencing (correction) purposes in XPS analysis: Insights from a multi-user facility data review. *Applied Surface Science* **2022**, *597*, 153681.

(50) Feng, Y.; Koo, B. M.; Seyeux, A.; Światowska, J.; Henry de Villeneuve, C.; Rosso, M.; Ozanam, F. ToF-SIMS Li Depth Profiling of Pure and Methylated Amorphous Silicon Electrodes After Their Partial Lithiation. *ACS Applied Materials & Interfaces* **2022**, *14*, 35716–35725, PMID: 35882598.

(51) Wan, T. H.; Saccoccio, M.; Chen, C.; Ciucci, F. Influence of the Discretization Methods on the Distribution of Relaxation Times Deconvolution: Implementing Radial Basis Functions with DRTtools. *Electrochimica Acta* **2015**, *184*, 483–499.

(52) Newville, M.; Stensitzki, T.; Allen, D. B.; Rawlik, M.; Ingargiola, A.; Nelson, A. LMFIT: Non-linear least-square minimization and curve-fitting for Python. *Astrophysics Source Code Library* **2016**, ascl–1606.

(53) Orazem, M. E.; Frateur, I.; Tribollet, B.; Vivier, V.; Marcelin, S.; Pébère, N.; Bunge, A. L.; White, E. A.; Riemer, D. P.; Musiani, M. Dielectric properties of materials showing constant-phase-element (CPE) impedance response. *Journal of The Electrochemical Society* **2013**, *160*, C215.

(54) Zhang, D.; Machala, M. L.; Chen, D.; Guan, Z.; Li, H.; Nemsak, S.; Crumlin, E. J.; Bluhm, H.; Chueh, W. C. Hydroxylation and Cation Segregation in (La 0.5 Sr 0.5)FeO 3-δ Electrodes . *Chemistry of Materials* **2020**, *32*, 2926–2934.

(55) Sunding, M. F.; Hadidi, K.; Diplas, S.; Løvvik, O. M.; Norby, T. E.; Gunnæs, A. E. XPS characterisation of in situ treated lanthanum oxide and hydroxide using tailored charge referencing and peak fitting procedures. *Journal of Electron Spectroscopy and Related Phenomena* **2011**, *184*, 399–409.

(56) Hiebl, C.; Young, D.; Wagner, R.; Wilkening, H. M.; Redhammer, G. J.; Rettenwander, D. Proton Bulk Diffusion in Cubic Li 7 La 3 Zr 2 O 12 Garnets as Probed by Single X-ray Diffraction. *Journal of Physical Chemistry C* **2019**, *123*, 1094–1098.

(57) Smetaczek, S.; Limbeck, A.; Zeller, V.; Ring, J.; Ganschow, S.; Rettenwander, D.; Fleig, J. Li+/H+ exchange of Li7La3Zr2O12 single and polycrystals investigated by quantitative LIBS depth profiling. *Materials Advances* **2022**, *46*, 8760–8770.

(58) Eckhardt, J. K.; Klar, P. J.; Janek, J.; Heiliger, C. Interplay of Dynamic Constriction and Interface Morphology between Reversible Metal Anode and Solid Electrolyte in Solid State Batteries. *ACS Applied Materials & Interfaces* **2022**, *14*, 35545–35554.

(59) Tenhaeff, W. E.; Rangasamy, E.; Wang, Y.; Sokolov, A. P.; Wolfenstine, J.; Sakamoto, J.; Dudney, N. J. Resolving the Grain Boundary and Lattice Impedance of Hot-Pressed Li7La3Zr2O12 Garnet Electrolytes. *ChemElectroChem* **2014**, *1*, 375–378.

(60) Krauskopf, T.; Dippel, R.; Hartmann, H.; Peppler, K.; Mogwitz, B.; Richter, F. H.; Zeier, W. G.; Janek, J. Lithium-Metal Growth Kinetics on LLZO Garnet-Type Solid Electrolytes. *Joule* **2019**, *3*, 2030–2049.

(61) Wang, M. J.; Choudhury, R.; Sakamoto, J. Characterizing the Li-Solid-Electrolyte Interface Dynamics as a Function of Stack Pressure and Current Density. *Joule* **2019**, *3*, 2165–2178.

(62) Pesci, F. M.; Bertei, A.; Brugge, R. H.; Emge, S. P.; Hekselman, A. K.; Marbella, L. E.; Grey, C. P.; Aguadero, A. Establishing Ultralow Activation Energies for Lithium Transport in Garnet Electrolytes. *ACS Applied Materials and Interfaces* **2020**, *12*, 32806–32816.

(63) Eckhardt, J. K.; Fuchs, T.; Burkhardt, S.; Klar, P. J.; Janek, J.; Heiliger, C. Guidelines for Impedance Analysis of Parent Metal Anodes in Solid-State Batteries and the Role of Current Constriction at Interface Voids, Heterogeneities, and SEI. *Advanced Materials Interfaces* **2023**, *2202354*.

(64) Brugge, R. H.; Chater, R. J.; Kilner, J. A.; Aguadero, A. Experimental determination of Li diffusivity in LLZO using isotopic exchange and FIB-SIMS. *JPhys Energy* **2021**, *3*.

(65) Gombotz, M.; Hiebl, C.; Stainer, F.; Wilkening, H. M. R. Relaxation. **2023**, 6–13.

(66) Becking, J.; Gröbmeyer, A.; Kolek, M.; Rodehorst, U.; Schulze, S.; Winter, M.; Bieker, P.; Stan, M. C. Lithium-Metal Foil Surface Modification: An Effective Method to Improve the Cycling Performance of Lithium-Metal Batteries. *Advanced Materials Interfaces* **2017**, *4*, 1–9.

(67) Otto, S. K.; Moryson, Y.; Krauskopf, T.; Peppler, K.; Sann, J.; Janek, J.; Henss, A. In-Depth Characterization of Lithium-Metal Surfaces with XPS and ToF-SIMS: Toward Better Understanding of the Passivation Layer. *Chemistry of Materials* **2021**, *33*, 859–867.

(68) Flatscher, F.; Philipp, M.; Ganschow, S.; Wilkening, H. M. R.; Rettenwander, D. The natural critical current density limit for Li7La3Zr2O12garnets. *Journal of Materials Chemistry A* **2020**, *8*, 15782–15788.

(69) Fuchs, T.; Mogwitz, B.; Otto, S. K.; Passerini, S.; Richter, F. H.; Janek, J. Working Principle of an Ionic Liquid Interlayer During Pressureless Lithium Stripping on Li6.25Al0.25La3Zr2O12 (LLZO) Garnet-Type Solid Electrolyte. *Batteries and Supercaps* **2021**, *4*, 1145–1155.

TOC Graphic

Some journals require a graphical entry for the Table of Contents. This should be laid out "print ready" so that the sizing of the text is correct.

Inside the `tocentry` environment, the font used is Helvetica 8 pt, as required by *Journal of the American Chemical Society*.

The surrounding frame is 9 cm by 3.5 cm, which is the maximum permitted for *Journal of the American Chemical Society* graphical table of content entries. The box will not resize if the content is too big: instead it will overflow the edge of the box.

This box and the associated title will always be printed on a separate page at the end of the document.